

6 This draft manuscript is distributed solely for purposes of scientific peer review. Its content
7 is deliberative and predecisional, so it must not be disclosed or released by reviewers.
8 Because the manuscript has not yet been approved for publication by the U.S. Geological
9 Survey (USGS), it does not represent any official USGS finding or policy.

Abstract

Numerical simulations of Sequences of Earthquakes and Aseismic Slip (SEAS) have made great progress over the past decades to address important questions in earthquake physics and fault mechanics. However, significant challenges in SEAS modeling remain in resolving multiscale interactions between aseismic fault slip, earthquake nucleation, and dynamic rupture; and understanding physical factors controlling observables such as seismicity and ground deformation. The increasing capability and complexity of SEAS modeling calls for extensive efforts to verify codes and advance these simulations with rigor, reproducibility, and broadened impact. In 2018, we initiated a community code-verification exercise for SEAS simulations, supported by the Southern California Earthquake Center (SCEC). Here we report the findings from our first two benchmark problems (BP1 and BP2), designed to test the capabilities of different computational methods in correctly solving a mathematically well-defined, basic problem in crustal faulting. These benchmarks are for a 2D antiplane problem, with a 1D planar vertical strike-slip fault obeying rate-and-state friction, embedded in a 2D homogeneous, linear elastic half-space. Sequences of quasi-dynamic earthquakes with periodic occurrences (BP1) or bimodal sizes (BP2) and their interactions with aseismic slip are simulated. The comparison of >70 simulation results from 11 groups using different numerical methods, uploaded to our online platform, show excellent agreements in long-term and coseismic evolution of fault properties. In BP1, we found that the truncated domain boundaries influence interseismic fault stressing, earthquake recurrence, and coseismic rupture process, and that agreement between models is only achieved with sufficiently large domain sizes. In BP2, we found that complexity of long-term fault behavior depends on how well important physical length scales related to spontaneous nucleation and rupture propagation are resolved. Poor numerical resolution can result in the generation of artificial complexity, impacting simulation results that are of potential interest for characterizing seismic hazard, such as earthquake size distributions, moment release, and earthquake recurrence times. These results inform the development of more advanced SEAS models, contributing to our further understanding of earthquake system

Introduction and Motivation

When we develop models of physical systems, credible and reproducible results are essential to scientific progress. Robust predictive models of earthquake source processes have become important means for studying fundamental questions in earthquake science. Models of single earthquakes (known as *dynamic rupture simulations*) have emerged as powerful tools for understanding the influence of fault geometry, friction and prestress on rupture propagation, and for explaining observations of high-frequency ground motions and damage zones (Day, 1982; Olsen et al., 1997; Nielsen et al., 2000; Duan and Oglesby, 2006; Ripperger et al., 2007; Bhat et al., 2007; Dunham et al., 2011a,b; Lozos et al., 2011; Gabriel et al., 2012; Shi and Day, 2013; Kozdon and Dunham, 2013; Xu et al., 2015; Wollherr et al., 2018; Ma and Elbanna, 2019). Many of the codes used for these studies incorporate advanced features such as 3D domains and complex fault geometries, leading to very large problems for which rigorous convergence tests can be too computationally expensive. An alternative means for verifying model results are code comparisons made across the different modeling groups, using cell sizes at the limit of computational feasibility. Over the past decade, the SCEC/USGS Spontaneous Rupture Code Verification Project has made significant progress in using code comparison studies to provide confidence in model outcomes (Harris et al., 2009; Barall and Harris, 2015; Harris et al., 2018).

Although these dynamic rupture simulations have contributed greatly to our understanding of the physical factors that govern ground motion, they are limited to single-event scenarios with imposed artificial prestress conditions and *ad hoc* nucleation procedures. In order to understand earthquake source processes and how fault slip history influences subsequent events, it has been widely recognized that we need models that simulate behavior over multiple seismic events and the intervening periods of aseismic deformation. To address this need, models of Sequences of Earthquakes and Aseismic Slip (SEAS) have emerged that consider all phases of earthquake faulting, from slow tectonic loading to earthquake nucleation (under self-consistent prestress

68 conditions), propagation and termination. However, so far codes for SEAS simulations
69 remain untested. Inspired by the success of the SCEC/USGS Spontaneous Rupture
70 Code Verification Project, this paper describes the efforts of the SEAS initiative – a
71 SCEC (Southern California Earthquake Center) funded working group who has initi-
72 ated the first code-verification study for earthquake sequence simulations. In this pa-
73 per, we present the initial benchmark problems and results from the code comparisons
74 submitted to our online platform (<http://sceccdata.usc.edu/cvws/seas/>). Through
75 these exercises, we aim to provide confidence in SEAS model outcomes, determine best
76 practices for improvement of accuracy and efficiency of SEAS simulations, and provide
77 other scientists strategies for verification during code development.

78 In SEAS models the goal is to capture the interplay of interseismic periods and
79 the associated aseismic fault slip that ultimately lead to earthquake nucleation and
80 earthquakes (dynamic rupture events) themselves, in an effort to understand which
81 physical factors control the full range of observables such as aseismic deformation,
82 nucleation locations of earthquakes, ground shaking during dynamic rupture, recurrence
83 times and magnitudes of major earthquakes, see Figure 1. These features distinguish
84 SEAS models from both dynamic rupture models which only consider single events,
85 and the so-called earthquake simulators (*Tullis et al.*, 2012). Earthquake simulators are
86 capable of simulating seismicity patterns over millennium time scales in complex fault
87 network systems (*Richards-Dinger and Dieterich*, 2012) but are missing key physical
88 features that could potentially dominate earthquake and fault interaction, such as stress
89 transfer generated by dynamic waves, aseismic slip within fault segments, and inelastic
90 responses.

91 SEAS modeling is not without significant challenges, due to the varying tempo-
92 ral and spatial scales that characterize earthquake source behavior. For computational
93 efficiency the vast majority of SEAS models do not consider full dynamics during earth-
94 quake rupture, but rather take a "quasi-dynamic" approach, where inertia is only ap-
95 proximated (see section for further details). Computations are further complicated
96 when material heterogeneities, bulk inelastic responses and fault nonplanarity are in-

97 cluded. However, accounting for such complexity is widely recognized as crucial for
98 understanding the real Earth and predicting seismic hazards. Significant developments
99 in SEAS models over the past decade have incorporated some of these complexities and
100 connected model outcomes to geophysical observations. For example, seismological and
101 geodetic observations have been combined with modeling of coseismic and quasi-static
102 (aseismic) deformation to infer the spatial distribution of fault frictional properties
103 (*Johnson et al.*, 2006; *Barbot et al.*, 2009; *Mitsui and Hirahara*, 2011; *Dublanchet et al.*,
104 2013; *Floyd et al.*, 2016; *Jiang and Fialko*, 2016), the decay rate of aftershocks (*Per-
105 fettini and Avouac*, 2004, 2007), the role of tremor and slow slip (*Mele Veedu and
106 Barbot*, 2016; *Dublanchet*, 2017; *Luo and Ampuero*, 2017), and long-term models have
107 been used to reproduce characteristics of multiple and/or repeating events (*Chen and
108 Lapusta*, 2009; *Barbot et al.*, 2012). The framework of earthquake cycle modeling is
109 also adopted to explain geodetic and geologic data (*Meade et al.*, 2013; *Kaneko et al.*,
110 2011; *Wei et al.*, 2013, 2018), study subduction zones (*Hori et al.*, 2004; *van Dinther
111 et al.*, 2013; *Noda and Lapusta*, 2013; *Liu and Rice*, 2005, 2007; *Li and Liu*, 2016,
112 2017), collision zones (*Qiu et al.*, 2016; *Michel et al.*, 2017), and explore induced seis-
113 micity phenomena (*McClure and Horne*, 2011; *Dieterich et al.*, 2015), among many
114 applications.

115 While SEAS models are being used to explain, reproduce, and predict earthquake
116 behavior and other geophysical phenomena, a critical step must be to ensure that these
117 methodologies are accurate. The SEAS initiative is also taking the step to improve
118 and promote a new generation of verified numerical SEAS models that can simulate
119 much longer periods of earthquake activity than single-event dynamic rupture simula-
120 tions but with the same level of computational rigor, while incorporating qualitatively
121 different features such as (a) pre-, inter-, and post-seismic slip and the resulting stress
122 redistribution, (b) spontaneous earthquake nucleation, and (c) physical processes rele-
123 vant to long-term slip such as interseismic healing of the fault zone, viscoelasticity, and
124 fluid flow. Such SEAS models can provide physics-based approximations for larger-scale
125 and longer-term earthquake simulators. In addition they can inform the initial condi-

126 tions and nucleation procedures for dynamic rupture simulations, however our vision
127 for SEAS models is to develop them all to include full dynamic ruptures, capturing the
128 range of processes and heterogeneities known to be essential for realistic ground motion
129 modeling.

130 SEAS Modeling Challenges and Initial Benchmark 131 Problems

132 Although the ultimate SEAS modeling framework would naturally include dynamic rup-
133 ture modeling, current methods for simulating SEAS problems require computational
134 codes that are fundamentally different from those used in single-event dynamic rupture
135 simulations. The use of variable time stepping and possible switching between different
136 computational schemes is required in order to resolve sub-seconds to year-long changes.
137 The interaction between the highly nonlinear nature of the problems and round-off er-
138 rors can lead to model divergence. The need to distinguish between legitimate solution
139 differences due and improper choices of algorithm and modeling procedures necessitates
140 new and more suitable comparison metrics.

141 SEAS models are unique in that they cover a wide range of numerical methodologies
142 and applications in earthquake science. Methods based on spectral boundary integral
143 formulations (BIEM) are efficient in solving for earthquake ruptures with quasi-dynamic
144 or full inertial effects (*Lapusta and Rice, 2003; Lapusta and Liu, 2009; Jiang and La-*
145 *pusta, 2016*). Methods based on the finite difference method (FDM) or a hybrid finite
146 element/spectral BIEM have been used to simulate quasi-dynamic ruptures on faults
147 with more complex bulk rheologies (*Erickson and Dunham, 2014; Erickson et al., 2017;*
148 *Allison and Dunham, 2018; Mckay et al., 2019; Abdelmeguid et al., 2019*). Other SEAS
149 modeling approaches include boundary element methods (BEM) for simulating slow slip
150 and tremor (e.g., *Tse and Rice, 1986; Rice and Tse, 1986; Ong et al., 2019; Goswami*
151 *and Barbot, 2018; Luo and Ampuero, 2011; Nakata et al., 2012; Liu, 2013; Wei et al.,*

2013), coupling faulting with fluid/heat transport and inelastic dilatancy (*Segall and Bradley, 2012a*), effects of surface topography (*Ohtani and Hirahara, 2015*), frictional heterogeneities (*Kato, 2016*) and viscoelastic response (*Kato, 2002; Lambert and Barbot, 2016; Barbot, 2018*). A spectral element method (SEM) has also been developed for simulating fully dynamic earthquakes in a heterogeneous bulk (*Kaneko et al., 2010*).

To verify the accuracy of SEAS models based on these different computational methods, the SEAS group developed our first benchmark problem, BP1, to test the capabilities of different computational methods in correctly solving a mathematically well-defined problem in crustal faulting. The overall strategy of our benchmark exercises is to produce robust results and maximize participation, with the goal of obtaining agreements in resolving detailed fault slip history over a range of time scales. These efforts required us to better understand the dependence of fault slip history on initial conditions, model spin-up, fault properties, and friction laws. Given the complexity of this task, it was important to start from the most basic problem and gradually add model complexity. BP1 is a 2D antiplane problem, with a 1D planar vertical strike-slip fault embedded in a 2D homogeneous, linear elastic half-space with a free surface, see Figure 2. Full details of this benchmark (and subsequent benchmarks), including governing equations and initial and fault interface conditions, are available online on the SEAS platform (<http://scecddata.usc.edu/cvws/seas/index.html>). We include some of the details on the friction law here, for clarity of important concepts.

The fault is governed by rate- and state-dependent friction (*Dieterich, 1979; Ruina, 1983; Marone, 1998*) where shear stress on the fault τ is set equal to fault strength F , namely

$$\tau = F(V, \theta), \tag{1}$$

where $\tau = \tau^0 + \tau^{\text{qs}} - \eta V$ is the sum of the prestress τ^0 , the shear stress due to quasi-static deformation τ^{qs} , and the radiation damping term $-\eta V$ as approximation to inertia (*Rice, 1993*). $\eta = \mu/2c_s$ is half the shear-wave impedance for shear wave speed $c_s = \sqrt{\mu/\rho}$, where μ is the elastic shear modulus and ρ is the material density. The

180 fault strength $F = \sigma_n f(V, \theta)$, where V is the slip rate and θ is a state variable. σ_n is
 181 the effective normal stress on the fault. For this first benchmark problem we assume θ
 182 evolves according to the aging law

$$183 \quad \frac{d\theta}{dt} = 1 - \frac{V\theta}{L}, \quad (2)$$

184 where L is the critical slip distance. The friction coefficient f is given by a regularized
 185 formulation (*Lapusta et al.*, 2000)

$$186 \quad f(V, \theta) = a \sinh^{-1} \left[\frac{V}{2V_0} \exp \left(\frac{f_0 + b \ln(V_0\theta/L)}{a} \right) \right] \quad (3)$$

187 for reference friction coefficient f_0 and reference slip rate V_0 . Depth-dependent fric-
 188 tional parameters a and b define a shallow seismogenic region with velocity-weakening
 189 (VW) friction and a deeper velocity-strengthening (VS) region, below which a rela-
 190 tive plate motion rate is imposed. A periodic sequence of spontaneous, quasi-dynamic
 191 earthquakes and slow slip are simulated in the model, see Figure 3a, where results from
 192 the BICyclE code (*Lapusta et al.*, 2000; *Lapusta and Liu*, 2009) show slip contours plot-
 193 ted against fault depth in blue every 5 yr during interseismic loading and in red every
 194 1 s during the coseismic phase. Over a 1200 year simulation period, approximately 13
 195 events take place, nucleating at a depth of ~ 12 km, rupturing to a depth of ~ 18 km,
 196 and accumulating ~ 3 m of slip at the Earth’s surface. Model parameters used for the
 197 benchmark are given in Table 1.

198 A critical physical length scale present in this first benchmark problem, often re-
 199 ferred to as the process zone or cohesive zone Λ , describes the spatial region near the
 200 rupture front under which breakdown of fault resistance occurs, and shrinks as ruptures
 201 propagate faster (*Palmer and Rice*, 1973). For fault models governed by rate-and-state
 202 friction, the quasi-static process zone at a rupture speed of 0^+ , Λ_0 , can be estimated
 203 (*Day et al.*, 2005; *Ampuero and Rubin*, 2008; *Perfettini and Ampuero*, 2008) as

$$204 \quad \Lambda_0 = C \frac{\mu L}{b\sigma_n}, \quad (4)$$

205 where C is a constant of order 1. Another characteristic length scale which has been
 206 shown to control model behavior is the critical nucleation size h^* , which governs the
 207 minimum extent of the rate-weakening region under which spontaneous nucleation may
 208 occur, (see *Andrews, 1976a,b; Rubin and Ampuero, 2005; Ampuero and Rubin, 2008*).
 209 For 2D problems, the critical nucleation size can be estimated for the aging law (with
 210 $0.5 < a/b < 1$) as

$$211 \quad h^* = \frac{2}{\pi} \frac{\mu b L}{(b - a)^2 \sigma_n}. \quad (5)$$

212 A cell size of 50 m was used for BP1, resolving Λ_0 with approximately 6 grid points and
 213 h^* with approximately 40 grid points.

214 We developed the second benchmark BP2 that is similar to BP1 to explore the
 215 model resolution issues, which will be important in future benchmarks in 3D when
 216 computational efficiency demands a larger cell size. Complexity of event sizes and
 217 recurrence times is known to emerge through a reduction in the characteristic slip
 218 distance L (*Lapusta and Rice, 2003; Mitsui and Hirahara, 2011; Wu and Chen, 2014;*
 219 *Kato, 2014; Barbot, 2019; Viesca, 2016a,b; Cattania, 2019*). Thus BP2 is exactly the
 220 same as BP1 except that L is halved, resulting in bimodal sequences of full and partial
 221 ruptures of the velocity-weakening region (every large event is accompanied by a smaller
 222 event and the sequence repeats periodically). Besides aiming for agreements between
 223 different models, one main objective is to understand complexity in simulated events
 224 and how to deal with numerical resolution issues. A reduction in L corresponds to a
 225 reduction in the quasi-static process zone size Λ_0 . BP2 requests model outputs using
 226 a cell size of 25 m, 50 m, 100 m, 200 m, 300 m, 400 m and 800 m. The first three cases
 227 resolve Λ_0 with approximately 6, 3, and 1.7 grid points, and the other four cases do
 228 not resolve Λ_0 . Figures 3b-d show results from the BICycle code using a cell size of
 229 25 m, 100 m and 200 m respectively. Small cell sizes of 25 m and 50 m (the latter is not
 230 shown) show nearly indistinguishable, bimodal patterns of events nucleating at ~ 15 km
 231 depth, suggesting model convergence. A cell size of 100 m leads to a resolution issue
 232 where periodic behavior is observed, but the bimodal sequence of events is replaced by

233 an alternating sequence of large, small and medium sized events. A cell size of 200 m,
234 which does not resolve the process zone, reveals a loss of periodic behavior altogether
235 in favor of a broad range of event sizes and nucleation locations.

236 Modeling Groups and Working Platforms

237 For these benchmark exercises, we have used two SCEC-funded workshops (hosted in
238 April and November 2018, [http://scecddata.usc.edu/cvws/seas/workshop_presentations.](http://scecddata.usc.edu/cvws/seas/workshop_presentations.html)
239 [html](http://scecddata.usc.edu/cvws/seas/workshop_presentations.html)) as open platforms for modelers to share and follow recent scientific progress in the
240 field, discuss details in benchmark design/results, and collectively decide the directions
241 of our future efforts, with considerable inputs from students and early career scientists.
242 Over 10 modeling groups participated in these first two benchmarks; the details of the
243 group members and different computational methods are summarized in Table . Note
244 that the modeler name refers to the member of the modeling group who uploaded the
245 data to the platform for simulations done by the group. It does not necessarily refer to
246 the code author(s) - see the references in Table for authorship and code availability. For
247 time-stepping schemes, the majority of groups used adaptive Runge-Kutta methods for
248 both benchmark problems (the details of which can be found in the references listed in
249 Table), with the exception of QDYN, which applies a Bulirsch-Stoer method for BP1,
250 and BICycle, which incorporates adaptive time-stepping based on stability conditions
251 derived from the choice of constitutive relationship.

252 To facilitate the submission and comparison of simulation results, we established an
253 online platform that provides access to community resources and supports the submis-
254 sion, storage, visualization, and comparison of benchmark results, see Figure 4. For our
255 first benchmarks, we adopted a platform with similar functionality developed for the
256 SCEC dynamic rupture simulation group (<http://scecddata.usc.edu/cvws/seas/>).
257 All modelers can upload and immediately plot time-series data to quickly assess the
258 overall agreements between models for the time evolution of fault slip, slip rates and
259 shear stress at representative locations on fault. We use the online platform for prelim-

260 inary model comparisons and analyze more detailed model observables to verify these
261 computational codes.

262 Model Comparisons and What We Learned

263 It is important to note that the problem descriptions for BP1 and BP2 consider a semi-
264 infinite half-space. Codes based on a volume discretization (FDM/FEM) therefore had
265 to make their own decisions regarding computational domain truncation and far-field
266 boundary conditions. The figures in the following sections contain labels generated
267 by the platform which state the model group name and correspond to results from a
268 particular model set-up. Some results are followed by the version corresponding to an
269 alternative set-up, e.g. **abrahams.3** corresponds to results from the **abrahams** group
270 with an increased computational domain size of $(L_x, L_z) = (400 \text{ km}, 200 \text{ km})$ and a
271 remote displacement boundary condition, see the lower right of Figure 4. We discuss
272 in the next sections the implications that these choices had on model comparisons.

273 Results from BP1

274 For the first benchmark problem, BP1, we found qualitative agreements in nucleation
275 sites, depth extent of rupture, and slip with depth similar to those exemplified by the
276 slip contours in Figure 3a. In Figure 5 we plot time series of local shear stress and
277 slip rates at mid-seismogenic depth ($z = 7.5 \text{ km}$) from BP1 over the first 700 years for
278 different model results. Results from several BEM codes as well as codes with volume
279 discretization (**abrahams** and **kozdon** modeling groups) and varying computational
280 domain sizes are compared in Figure 5a-b. The legends indicate the computational
281 domain size and boundary condition. For BEM codes, HS refers to a half-space, and
282 $(L_z, \text{boundary condition})$ refers to computational domain depth and boundary condi-
283 tion, where BC3 corresponds to a periodic boundary condition. For codes with a vol-
284 ume discretization, $(L_x/L_z/\text{boundary condition})$, provides the computational domain
285 size used and BC1 and BC2 refers to a far-field free surface or a far-field displacement

286 boundary condition, respectively.

287 Figure 5(a-b) show model results from a BEM simulation (**liu**, in black) along with
288 four model results from volume discretization codes, revealing quantitative differences
289 in interevent times and peak values. Interevent times for different models range from
290 approximately 78.3 to 78.8 years over the whole 3000 year simulation period, leading
291 to model divergence at a near-constant rate. We found that these discrepancies were
292 caused by choices in domain truncation and boundary conditions. We were surprised to
293 find that far-field boundary condition type leads to quantitative differences in long-term
294 fault behavior for relatively small domains (revealed by the blue and orange curves).
295 This in part is due to small differences in the physical problem being solved by im-
296 plementations that use periodic or finite domain boundary conditions compared to the
297 spatial domain BEM methods which represent a truly infinite domain, and therefore
298 larger loading regions. The green and red curves show how the discrepancy in long-term
299 behavior among computational methodologies decreases as the physical domain size is
300 increased, suggesting convergence of results across the modeling groups. Figure 5(c-d)
301 shows comparisons of all models with $L_z > 160$ km, further illustrating that excellent
302 agreements between model results can be achieved with sufficiently large domain sizes.

303 While computational domain size and boundary conditions can lead to model diver-
304 gence over the long term, the coseismic behavior of individual earthquake are qualita-
305 tively well reproduced by all models. In Figure 6 we show the time series of shear stress
306 evolution near the nucleation depth (12.5 km) and slip rate (at a mid-seismogenic depth
307 of 7.5 km) during the coseismic phase for the 8th event in the sequence from Figure 5.
308 We chose these plotting depths as they best illustrate model discrepancies, with time
309 series aligned relative to the rupture initiation time at the depth of 12.5 km. Peak val-
310 ues in slip rates at 7.5 km depth occur approximately 10 s later, and co-seismic surface
311 reflection phases are marked for all four plots with black arrows. Figures 6(a-b) show
312 results from models on relatively small computational domains, revealing discrepan-
313 cies in pre-rupture stress levels near the locked-creeping transition due to differences
314 in interseismic loading, and resultant coseismic rupture behavior, including peak shear

315 stress and rupture speeds as evidenced by rupture initiation times of the direct and
316 surface-reflection phases at depth of 7.5 km. Figures 6(c-d) illustrate excellent agree-
317 ments for model results on larger domains. The discrepancy of <1 MPa in prestress
318 levels at transitional depths does not result in pronounced difference in fault slip rate
319 evolution.

320 Results from BP2

321 For BP2 we suggested submissions of multiple models with different spatial resolutions
322 from each group, see Table . By design, models with a cell size/node spacing that does
323 not resolve critical length scales – process zone size and nucleation zone size defined in
324 (4) and (5) – would produce increased complexity in earthquake sequences, observed
325 previously (*Rice, 1993; Ben-Zion and Rice, 1997; Day et al., 2005; Lapusta and Liu,*
326 *2009*), and illustrated in the cumulative slip profiles in Figure 3(b-d).

327 While drastic differences in small event patterns arise for large cell sizes, we found
328 that with increasing resolution results converge to an alternating sequence of large and
329 small events among most models. Figure 7a shows the long term evolution of slip rates
330 at 9.6 km (near the bottom of the seismogenic zone and above the earthquake initiation
331 depth) for the best model results (with a cell size of 25 m and large computational
332 domain sizes). We found that even models with similar cell/domain sizes tend to
333 produce results that are initially closely matching, but diverge over time, likely due to
334 accumulation of numerical round-off errors and differences in computational techniques.
335 However, if we zoom in on the tenth event in the sequence (gray bar in Figure 7a), the
336 time series of fault slip rates, aligned with respect to the start time of seismic slip
337 at the depth of 12 km within each model, show good agreements (Figure 7b). While
338 small discrepancies exist in peak slip rates and early source complexity, partly due
339 to differences in interevent times, the models with the highest resolution exhibit good
340 agreements in their overall coseismic behavior despite their divergence in the long term.

341 Figure 8 illustrates how model agreement is gradually lost with decreased model
342 resolution. For cell sizes of 25 m and 50 m, long-term stress evolution near the locked-

343 creeping transition is qualitatively similar for the three models shown and the offset
 344 in the timing of earthquakes does not significantly affect coseismic behavior of major
 345 events, as indicated by comparable coseismic stress drops. For large cell sizes of 100 m
 346 and 200 m, not only is the time offset more random, but also coseismic stress drops and
 347 event patterns vary between models. Numerical artifacts and different computational
 348 techniques likely contribute to the divergence of simulation results.

349 In Figure 9 we plot the distribution of earthquake sizes, seismic moment release and
 350 frequency-size relation for two groups of models (**jiang** and **cattania**) with increasing
 351 cell sizes. For the 2D problem, we define earthquake size as moment release per length
 352 for each event, $M = \int \mu s dz$, where shear modulus $\mu = c_s^2 \rho \approx 32$ GPa and s is total
 353 coseismic slip over the cell. While better resolved models (cell sizes of 25 m and 50 m)
 354 show excellent agreements between the two groups, models produce dramatically dif-
 355 ferent earthquake statistics when cell size increases to 400 m, with the most significant
 356 discrepancies in smaller earthquakes between the two models (Figure 9a). The distri-
 357 bution of total seismic moment release, M_t , calculated as the sum of moment release
 358 during all earthquakes within a certain magnitude range, also changes with cell sizes,
 359 though in a similar manner for the two model groups (Figure 9b). Overall, models with
 360 larger cell sizes tend to produce large earthquakes with reduced total moment; part of
 361 the moment deficit is accommodated through many more smaller earthquakes and the
 362 rest through additional aseismic slip. For example, the total moment release through
 363 largest earthquakes in 400-m models is only half of that in 25-m models. These results
 364 demonstrate that simulated small earthquakes are especially sensitive to model resolu-
 365 tion and large earthquake behavior can also be affected. In addition, Figure 9c reveals
 366 how different simulations with poor resolution can produce similar power-law features
 367 in frequency-size distributions over certain ranges of earthquake sizes, as a result of
 368 numerical artifacts rather than well-resolved physics.

369 In Figure 10 we illustrate the effect of model resolution on the partition between
 370 seismic and aseismic slip. Normalized seismic moment release R_s is plotted against
 371 depth for several modeling groups, in solid lines for total seismic moment release and

372 dashed lines for seismic moment due to surface-breaching events. $R_s = 0$ implies that
373 all plate motion is accommodated by aseismic slip on the fault, while $R_s = 1$ means that
374 all moment is released through earthquakes. A transitional zone in this partitioning
375 around $z = H$ and down to $z = H + h$ ($H = 15$ and $h = 3$ in this exercise) is evidenced
376 in the well-resolved models ($\Delta_z = 25, 50, 100$ m). The poorly resolved models, however,
377 illustrate model discrepancies in the seismic/aseismic partitioning, with the near-surface
378 slip budget being increasingly accommodated by small earthquakes and aseismic slip
379 with increased cell sizes.

380 In Figure 11 we show interevent times for large surface-breaching events for all
381 models and cell sizes, showing a strong agreement of ~ 110 years for a cell size of
382 25 m, with an increasing variability and discrepancies among models with increased cell
383 size. Although the range of earthquake recurrence intervals are highly dependent on
384 cell sizes, the median values across models with larger cell sizes do not significantly
385 deviate from the uniform recurrence intervals in well-resolved models. This suggests
386 that at least some observables in these models retain information of the true behavior
387 of physical models and the larger cell sizes can be viewed as a factor that leads to
388 increased modeling errors.

389 Conclusions and Perspectives

390 For the first two SEAS benchmarks we found that discrepancies among well-resolved
391 models were significantly influenced by computational domain size, with larger do-
392 mains yielding improvements in agreements, regardless of domain boundary conditions.
393 Spin-up periods (time required for system to be independent of initial conditions) for
394 well-resolved models was relatively short - approximately 2-3 events. Results on large
395 domains agree well initially but still diverge over time, which was not unexpected due
396 to accumulation of round-off errors and differences in computational techniques. For
397 BP2 we investigated model resolution and observed qualitative similarities of bimodal
398 events when the process zone was resolved by approximately 3 and 6 grid points, sug-

399 gesting model convergence. A failure to resolve this length scale however, can lead
400 to substantial differences in long-term fault behavior as well as earthquake statistics
401 relevant to seismic hazard, such as frequency-size distributions and interevent times.

402 Although our initial benchmarks have a simple setup, comparison of results for
403 tens of models have yielded some unexpected and important insights, affirming the
404 importance of starting simple in a community code verification exercise. The results
405 and lessons from our initial benchmarks prepare us for future benchmark problems that
406 incrementally incorporate additional, potentially dominating physical factors, including
407 fully dynamic ruptures, coupling with fluids, multiple fault segments, nonplanar fault
408 geometries, and inelastic bulk constitutive behavior (e.g., *Segall and Rice*, 1995; *Noda*
409 *and Lapusta*, 2010; *Segall and Rice*, 2006; *Segall et al.*, 2010; *Erickson et al.*, 2017;
410 *Lambert and Barbot*, 2016; *Qiu et al.*, 2016; *Barbot*, 2018; *Ong et al.*, 2019). For future
411 verification exercises, we plan to address important issues in SEAS simulations, such as
412 3D effects, heterogeneous fault frictional properties, and full dynamics, which should
413 advance the state-of-the-art computational capabilities in our field.

414 The goal of the SEAS initiative is to promote advanced models with robust physical
415 features—a large spectrum of rupture styles and patterns, including slow-slip events,
416 complex earthquake sequences, fluid effects, dynamic stress changes, and inelastic
417 deformation—that are currently missing in the large-scale, long-term earthquake sim-
418 ulator frameworks such as ViscoSim, RSQSIM, Virtual California, and ALLCAL (*Pol-*
419 *litz*, 2012; *Richards-Dinger and Dieterich*, 2012; *Sachs et al.*, 2012; *Ward*, 2012). This
420 new generation of verified SEAS models will help determine the controlling physical
421 mechanisms of earthquake nucleation, propagation, and arrest. The community-wide
422 initiative would also provide incentives and new ideas to characterize modeling uncer-
423 tainty for the increasingly complex earthquake source models, an important step in
424 using physics-based models for the assessment of seismic hazard. Future validation ef-
425 forts comparing physics-based models with geophysical observations will bridge studies
426 in paleoseismology, geodesy, and seismology to understand fault behavior over multiple
427 temporal and spatial scales.

428 **Data and Resources:** Our online platform (<http://scecddata.usc.edu/cvws/seas/>)
429 is being developed and maintained by M.B. The data for local fault properties are stored
430 on the platform.

431 **Author Contributions:** B.A.E. and J.J. designed the benchmark problems, analyzed
432 model results, co-organized the workshops and co-wrote this article. M.B. developed
433 and maintains the online platform. M.B., N.L., E.M.D. and R.H. provided major
434 support and advice in forming the working group, obtaining funding, and manuscript
435 writing. Remaining co-authors provided feedback on benchmark design, participated
436 in the benchmark exercises, helped revise the manuscript, and are listed alphabetically.

437
438 **Acknowledgments:** B.A.E., J.J. and M.B. were supported through the Southern Cal-
439 ifornia Earthquake Center, grant no. 18099 and 19109. Two SEAS-themed workshops
440 were funded by SCEC awards no. 17151 and 18102. SCEC is funded by NSF Coopera-
441 tive Agreement EAR-0529922 and USGS Cooperative Agreement 07HQAG0008. This
442 is SCEC contribution no. 9066.

References

- Abdelmeguid, M., X. Ma, and A. Elbanna, A novel hybrid finite element-spectral boundary integral scheme for modeling earthquake cycles: Application to rate and state faults with low-velocity zones, *J. Geophys. Res. (to appear)*, doi:10.31223/osf.io/xwhbs, 2019.
- Allison, K., and E. M. Dunham, Earthquake cycle simulations with rate-and-state friction and power-law viscoelasticity, *Tectonophysics*, 733, 232 – 256, doi:https://doi.org/10.1016/j.tecto.2017.10.021, 2018.
- Ampuero, J.-P., and A. M. Rubin, Earthquake nucleation on rate and state faults – Aging and slip laws, *J. Geophys. Res.-Sol. Ea.*, 113(B1), doi:10.1029/2007JB005082, 2008.
- Andrews, D. J., Rupture propagation with finite stress in antiplane strain, *J. Geophys. Res.*, 81, 3575–3582, 1976a.
- Andrews, D. J., Rupture velocity of plane strain shear cracks, *J. Geophys. Res.*, 81, 5679–5687, 1976b.
- Barall, M., and R. A. Harris, Metrics for comparing dynamic earthquake rupture simulations, *Seismol. Res. Lett.*, 86(1), doi:10.1785/0220140122, 2015.
- Barbot, S., Asthenosphere flow modulated by megathrust earthquake cycles, *Geophys. Res. Lett.*, 45, 6018–6031, doi:10.1029/2018GL078197, 2018.
- Barbot, S., Slow-slip, slow earthquakes, period-two cycles, full and partial ruptures, and deterministic chaos in a single asperity fault, *Tectonophysics*, doi:10.1016/j.tecto.2019.228171, 2019.
- Barbot, S., Y. Fialko, and Y. Bock, Postseismic deformation due to the Mw6.0 2004 Parkfield earthquake: Stress-driven creep on a fault with spatially variable rate-and-state friction parameters, *J. Geophys. Res.*, 114(B07405), doi:10.1029/2008JB005748, 2009.

469 Barbot, S., N. Lapusta, and J.-P. Avouac, Under the hood of the earthquake machine:
470 Toward predictive modeling of the seismic cycle, *Science*, 336(6082), 707–710, doi:
471 10.1126/science.1218796, 2012.

472 Ben-Zion, Y., and J. R. Rice, Dynamic simulations of slip on a smooth fault in an elastic
473 solid, *J. Geophys. Res.-Sol. Ea.*, 102(B8), 17,771–17,784, doi:10.1029/97JB01341,
474 1997.

475 Bhat, H. S., M. Olives, R. Dmowska, and J. R. Rice, Role of fault branches in earthquake
476 rupture dynamics, *J. Geophys. Res.*, 112(B11309), 16, doi:10.1029/2007JB005027,
477 2007.

478 Bradley, A. M., Software for efficient static dislocation–traction calculations in fault
479 simulators, *Seismol. Res. Lett.*, 85(6), 1358–1365, doi:10.1785/0220140092, 2014.

480 Cattania, C., Complex earthquake behavior on simple faults, *submitted to Geophys.*
481 *Res. Lett.*, doi:10.31223/osf.io/hgbjx, 2019.

482 Chen, T., and N. Lapusta, Scaling of small repeating earthquakes explained by inter-
483 action of seismic and aseismic slip in a rate and state fault model, *J. Geophys. Res.*,
484 114(B01311), doi:10.1029/2008JB005749, 2009.

485 Day, S. M., Three-dimensional finite difference simulation of fault dynamics: rectan-
486 gular faults with fixed rupture velocity, *Bull. Seismol. Soc. Am.*, 72(3), 705–727,
487 1982.

488 Day, S. M., L. A. Dalguer, N. Lapusta, and Y. Liu, Comparison of finite difference and
489 boundary integral solutions to three-dimensional spontaneous rupture, *J. Geophys.*
490 *Res.-Sol. Ea.*, 110(B12), doi:10.1029/2005JB003813, 2005.

491 Dieterich, J. H., Modeling of rock friction: 1. experimental results and constitutive equa-
492 tions, *J. Geophys. Res.-Sol. Ea.*, 84(B5), 2161–2168, doi:10.1029/JB084iB05p02161,
493 1979.

494 Dieterich, J. H., K. B. Richards-Dinger, and K. A. Kroll, Modeling injection-induced
495 seismicity with the physics-based earthquake simulator RSQSim, *Seismol. Res. Lett.*,
496 *86*(4), doi:10.1785/0220150057, 2015.

497 Duan, B., and D. D. Oglesby, Heterogeneous fault stresses from previous earthquakes
498 and the effect on dynamics of parallel strike-slip faults, *J. Geophys. Res.*, *111*(B5),
499 2006.

500 Dublanchet, P., The dynamics of earthquake precursors controlled by effective friction,
501 *Geophys. J. Int.*, *212*(2), 853–871, 2017.

502 Dublanchet, P., P. Bernard, and P. Favreau, Interactions and triggering in a 3-d rate-
503 and-state asperity model, *J. Geophys. Res.*, *118*(5), 2225–2245, 2013.

504 Dunham, E. M., D. Belanger, L. Cong, and J. E. Kozdon, Earthquake ruptures with
505 strongly rate-weakening friction and off-fault plasticity, Part:1: Planar faults, *Bull.*
506 *Seismol. Soc. Am.*, *101*(5), 2296–2307, doi:10.1785/0120100075, 2011a.

507 Dunham, E. M., D. Belanger, L. Cong, and J. E. Kozdon, Earthquake ruptures with
508 strongly rate-weakening friction and off-fault plasticity, Part:2: Nonplanar faults,
509 *Bull. Seismol. Soc. Am.*, *101*(5), 2308–2322, doi:10.1785/0120100076, 2011b.

510 Erickson, B. A., and E. M. Dunham, An efficient numerical method for earthquake
511 cycles in heterogeneous media: Alternating subbasin and surface-rupturing events on
512 faults crossing a sedimentary basin, *J. Geophys. Res.-Sol. Ea.*, *119*(4), 3290–3316,
513 doi:10.1002/2013JB010614, 2014.

514 Erickson, B. A., E. M. Dunham, and A. Khosravifar, A finite difference method for
515 off-fault plasticity throughout the earthquake cycle, *J. Mech. Phys. Solids*, *109*, 50 –
516 77, doi:10.1016/j.jmps.2017.08.002, 2017.

517 Floyd, M. A., et al., Spatial variations in fault friction related to lithology from rupture
518 and afterslip of the 2014 South Napa, California, earthquake, *Geophys. Res. Lett.*,
519 *43*(13), 6808–6816, doi:10.1002/2016GL069428, 2016.

520 Gabriel, A.-A., J.-P. Ampuero, L. A. Dalguer, and P. M. Mai, The transition of dynamic
521 rupture styles in elastic media under velocity-weakening friction, *J. Geophys. Res.*,
522 *117*(B9), 2012.

523 Goswami, A., and S. Barbot, Slow-slip events in semi-brittle serpentinite fault zones,
524 *Scientific reports*, *8*(1), 6181, 2018.

525 Harris, R. A., et al., The SCEC/USGS dynamic earthquake rupture code verification
526 exercise, *Seismol. Res. Lett.*, *80*, 119–126, doi:10.1785/gssrl.80.1.119, 2009.

527 Harris, R. A., et al., A suite of exercises for verifying dynamic earthquake rupture codes,
528 *Seismol. Res. Lett.*, *89*(3), doi:<https://doi.org/10.1785/0220170222>, 2018.

529 Hori, T., N. Kato, K. Hirahara, T. Baba, and Y. Kaneda, A numerical simulation of
530 earthquake cycles along the Nankai Trough in southwest Japan: Lateral variation in
531 frictional property due to the slab geometry controls the nucleation position, *Earth
532 Planet Sc. Lett.*, *228*(3-4), 215–226, 2004.

533 Jiang, J., and Y. Fialko, Reconciling seismicity and geodetic locking depths on the
534 Anza section of the San Jacinto fault, *Geophys. Res. Lett.*, *43*(20), 10,663–10,671,
535 doi:10.1002/2016GL071113, 2016.

536 Jiang, J., and N. Lapusta, Deeper penetration of large earthquakes on seismically qui-
537 escent faults, *Science*, *352*(6291), 1293–1297, doi:10.1126/science.aaf1496, 2016.

538 Johnson, K. M., R. Bürgmann, and K. Larson, Frictional properties of the San Andreas
539 Fault near Parkfield, California, inferred from models of afterslip following the 2004
540 earthquake, *Bull. Seismol. Soc. Am.*, *96*(4B), doi:10.1785/0120050808, 2006.

541 Kaneko, Y., J.-P. Avouac, and N. Lapusta, Towards inferring earthquake patterns from
542 geodetic observations of interseismic coupling, *Nat. Geosci.*, *3*, 2010.

543 Kaneko, Y., J.-P. Ampuero, and N. Lapusta, Spectral-element simulations of long-term
544 fault slip: Effect of low-rigidity layers on earthquake-cycle dynamics, *J. Geophys.
545 Res.-Sol. Ea.*, *116*(B10), doi:10.1029/2011JB008395, 2011.

546 Kato, N., Seismic cycle on a strike-slip fault with rate-and state-dependent strength
547 in an elastic layer overlying a viscoelastic half-space, *Earth Planets Space*, 54(11),
548 1077–1083, 2002.

549 Kato, N., Deterministic chaos in a simulated sequence of slip events on a single isolated
550 asperity, *Geophys. J. Int.*, 198(2), 727–736, 2014.

551 Kato, N., Earthquake cycles in a model of interacting fault patches: Complex behavior
552 at transition from seismic to aseismic slip, *Bull. Seismol. Soc. Am.*, 106(4), 1772–
553 1787, 2016.

554 Kozdon, J. E., and E. M. Dunham, Rupture to the trench: Dynamic rupture simulations
555 of the 11 March 2011 Tohoku earthquake, *Bull. Seismol. Soc. Am.*, 103(2B), 1275–
556 1289, doi:10.1785/0120120136, 2013.

557 Lambert, V., and S. Barbot, Contribution of viscoelastic flow in earthquake cycles
558 within the lithosphere-asthenosphere system, *Geophys. Res. Lett.*, 43(19), 142–154,
559 2016.

560 Lapusta, N., and Y. Liu, Three-dimensional boundary integral modeling of spontaneous
561 earthquake sequences and aseismic slip, *J. Geophys. Res.-Sol. Ea.*, 114(B9), doi:
562 10.1029/2008JB005934, 2009.

563 Lapusta, N., and J. R. Rice, Nucleation and early seismic propagation of small and
564 large events in a crustal earthquake model, *J. Geophys. Res.*, 108(B4, 2205), 2003.

565 Lapusta, N., J. R. Rice, Y. Ben-Zion, and G. Zheng, Elastodynamic analysis for slow
566 tectonic loading with spontaneous rupture episodes on faults with rate- and state-
567 dependent friction, *J. Geophys. Res.-Sol. Ea.*, 105(B10), 23,765–23,789, doi:10.1029/
568 2000JB900250, 2000.

569 Li, D., and Y. Liu, Spatiotemporal evolution of slow slip events in a nonplanar fault
570 model for northern Cascadia subduction zone, *J. Geophys. Res.*, 121(9), 6828–6845,
571 2016.

572 Li, D., and Y. Liu, Modeling slow-slip segmentation in Cascadia subduction zone con-
573 strained by tremor locations and gravity anomalies, *J. Geophys. Res.*, *122*(4), 3138–
574 3157, 2017.

575 Liu, Y., Numerical simulations on megathrust rupture stabilized under strong dilatancy
576 strengthening in slow slip region, *Geophys. Res. Lett.*, *40*(7), 1311–1316, doi:10.1002/
577 grl.50298, 2013.

578 Liu, Y., and J. R. Rice, Aseismic slip transients emerge spontaneously in three-
579 dimensional rate and state modeling of subduction earthquake sequences, *J. Geophys.*
580 *Res.*, *110*(B08307), doi:10.1029/2004JB003424, 2005.

581 Liu, Y., and J. R. Rice, Spontaneous and triggered aseismic deformation transients in a
582 subduction fault model, *J. Geophys. Res.*, *112*(B09404), doi:10.1029/2007JB004930,
583 2007.

584 Lozos, J. C., D. D. Oglesby, B. Duan, and S. G. Wesnousky, The effects of double fault
585 bends on rupture propagation: A geometrical parameter study, *Bull. Seismol. Soc.*
586 *Am.*, *101*(1), 385–398, 2011.

587 Luo, Y., and J. P. Ampuero, Numerical simulation of tremor migration triggered by
588 slow slip and rapid tremor reversals, *AGU Fall Meeting Abstracts*, S33C-02, 2011.

589 Luo, Y., and J. P. Ampuero, Preprint: Tremor migration patterns and the collective
590 behavior of deep asperities mediated by creep, doi:10.31223/osf.io/mbcav, 2017.

591 Ma, X., and A. Elbanna, Dynamic rupture propagation on fault planes with explicit
592 representation of short branches, *Earth Planet Sc. Lett.*, *523*, 115,702, doi:10.1016/j.
593 epsl.2019.07.005, 2019.

594 Marone, C., Laboratory-derived friction laws and their application to seismic faulting,
595 *Ann. Rev. Earth Pl. Sc.*, *26*(1), 643–696, doi:10.1146/annurev.earth.26.1.643, 1998.

596 McClure, M. W., and R. N. Horne, Investigation of injection-induced seismicity using a
597 coupled fluid flow and rate/state friction model, *Geophysics*, 76(6), WC181–WC198,
598 doi:10.1190/geo2011-0064.1, 2011.

599 Mckay, M. B., B. A. Erickson, and J. E. Kozdon, A computational method for earth-
600 quake cycles within anisotropic media, *Geophys. J. Int.*, doi:10.1093/gji/ggz320,
601 2019.

602 Meade, B. J., Y. Klinger, and E. A. Hetland, Inference of multiple earthquake-cycle
603 relaxation timescales from irregular geodetic sampling of interseismic deformation,
604 *Bull. Seismol. Soc. Am.*, 103(5), 2824–2835, doi:10.1785/0120130006, 2013.

605 Mele Veedu, M., and S. Barbot, The Parkfield tremors reveal slow and fast ruptures on
606 the same asperity, *Nature*, 532(7599), 361–365, doi:10.1038/nature17190, 2016.

607 Michel, S., J.-P. Avouac, N. Lapusta, and J. Jiang, Pulse-like partial ruptures and high-
608 frequency radiation at creeping-locked transition during megathrust earthquakes,
609 *Geophys. Res. Lett.*, 44(16), 8345–8351, doi:10.1002/2017GL074725, 2017.

610 Mitsui, Y., and K. Hirahara, Fault instability on a finite and planar fault related to
611 early phase of nucleation, *J. Geophys. Res.*, 116(B6), 2011.

612 Nakata, R., M. Hyodo, and T. Hori, Numerical simulation of afterslips and slow slip
613 events that occurred in the same area in Hyuga-nada of southwest Japan, *Geophys.*
614 *J. Int.*, 190(2), 1213–1220, doi:10.1111/j.1365-246X.2012.05552.x, 2012.

615 Nielsen, S. B., J. Carlson, and K. B. Olsen, Influence of friction and fault geometry on
616 earthquake rupture, *J. Geophys. Res.*, 105(B3), 6069–6088, 2000.

617 Noda, H., and N. Lapusta, Three-dimensional earthquake sequence simulations with
618 evolving temperature and pore pressure due to shear heating: Effect of heterogeneous
619 hydraulic diffusivity, *J. Geophys. Res.*, 115(B12314), doi:10.1029/2010JB007780,
620 2010.

621 Noda, H., and N. Lapusta, Stable creeping fault segments can become destructive as a
622 result of dynamic weakening, *Nature*, 493(7433), 518–521, 2013.

623 Ohtani, M., and K. Hirahara, Effect of the Earth’s surface topography on quasi-dynamic
624 earthquake cycles, *Geophys. J. Int.*, 203(1), 384–398, doi:10.1093/gji/ggv187, 2015.

625 Olsen, K. B., R. Madariaga, and R. J. Archuleta, Three-dimensional dynamic simulation
626 of the 1992 Landers earthquake, *Science*, 278(5339), 834–838, 1997.

627 Ong, M., Su Qing, S. Barbot, and J. Hubbard, Physics-based scenario of earthquake
628 cycles on the Ventura thrust system, California: The effect of variable friction and
629 fault geometry, *J. Pure Appl. Geophys.*, doi:10.1007/s00024-019-02111-9, 2019.

630 Palmer, A. C., and J. R. Rice, The growth of slip surfaces in the progressive failure of
631 over-consolidated clay, *Proc. Roy. Soc. Lond. A*, 332(1591), 527–548, doi:10.1098/
632 rspa.1973.0040, 1973.

633 Perfettini, H., and J.-P. Ampuero, Dynamics of a velocity strengthening fault region:
634 Implications for slow earthquakes and postseismic slip, *J. Geophys. Res.-Sol. Ea.*,
635 113(B9), doi:10.1029/2007JB005398, 2008.

636 Perfettini, H., and J.-P. Avouac, Postseismic relaxation driven by brittle creep: A possi-
637 ble mechanism to reconcile geodetic measurements and the decay rate of aftershocks,
638 application to the Chi-Chi earthquake, Taiwan, *J. Geophys. Res.*, 109(B02304), 2004.

639 Perfettini, H., and J.-P. Avouac, Modeling afterslip and aftershocks following the 1992
640 Landers earthquake, *J. Geophys. Res.*, 112(B07409), 2007.

641 Pollitz, F. F., ViscoSim Earthquake Simulator , *Seismol. Res. Lett.*, 83(6), 979–982,
642 doi:10.1785/0220120050, 2012.

643 Qiu, Q., et al., The mechanism of partial rupture of a locked megathrust: The role of
644 fault morphology, *Geology*, 44(10), 875–878, doi:10.1130/G38178.1, 2016.

645 Rice, J. R., Spatio-temporal complexity of slip on a fault, *J. Geophys. Res.*, *98*(B6),
646 9885–9907, 1993.

647 Rice, J. R., and S. T. Tse, Dynamic motion of a single degree of freedom system following
648 a rate and state dependent friction law, *J. Geophys. Res.*, *91*(B1), 521–530, 1986.

649 Richards-Dinger, K., and J. H. Dieterich, RSQSim earthquake simulator, *Bull. Seismol.*
650 *Soc. Am.*, *83*(6), 983–990, doi:<https://doi.org/10.1785/0220120105>, 2012.

651 Ripperger, J., J.-P. Ampuero, P. M. Mai, and D. Giardini, Earthquake source charac-
652 teristics from dynamic rupture with constrained stochastic fault stress, *J. Geophys.*
653 *Res.-Sol. Ea.*, *112*(B4), doi:10.1029/2006JB004515, 2007.

654 Rubin, A. M., and J.-P. Ampuero, Earthquake nucleation on (aging) rate and state
655 faults, *J. Geophys. Res.-Sol. Ea.*, *110*(B11), doi:10.1029/2005JB003686, 2005.

656 Ruina, A., Slip instability and state variable friction laws, *J. Geophys. Res.-Sol. Ea.*,
657 *88*(B12), 10,359–10,370, doi:10.1029/JB088iB12p10359, 1983.

658 Sachs, M. K., E. M. Heien, D. L. Turcotte, M. B. Yikilmaz, J. B. Rundle, and L. H.
659 Kellogg, Virtual California Earthquake Simulator, *Seismol. Res. Lett.*, *83*(6), 973–
660 978, doi:10.1785/0220120052, 2012.

661 Segall, P., and A. M. Bradley, The role of thermal pressurization and dilatancy in
662 controlling the rate of fault slip, *J. Appl. Mech.*, *79*(3), doi:10.1115/1.4005896, 2012a.

663 Segall, P., and A. M. Bradley, Slow-slip evolves into megathrust earthquakes in 2d nu-
664 merical simulations, *Geophys. Res. Lett.*, *39*(18), doi:10.1029/2012GL052811, 2012b.

665 Segall, P., and J. R. Rice, Dilatancy, compaction, and slip instability of a fluid infiltrated
666 fault, *J. Geophys. Res.*, *100*, 22,155–22,171, 1995.

667 Segall, P., and J. R. Rice, Does shear heating of pore fluid contribute to earthquake
668 nucleation?, *J. Geophys. Res.*, *111*(B09316), 17, 2006.

669 Segall, P., A. M. Rubin, A. M. Bradley, and J. R. Rice, Dilatant strengthening as a
670 mechanism for slow slip events, *J. Geophys. Res.*, 115(B12305), 2010.

671 Shi, Z., and S. M. Day, Rupture dynamics and ground motion from 3-d rough-fault
672 simulations, *J. Geophys. Res.-Sol. Ea.*, 118(3), 1122–1141, doi:10.1002/jgrb.50094,
673 2013.

674 Tse, S. T., and J. R. Rice, Crustal earthquake instability in relation to the depth
675 variation of frictional slip properties, *J. Geophys. Res.*, 91(B9), 9452–9472, 1986.

676 Tullis, T. E., et al., Generic earthquake simulator, *Seismol. Res. Lett.*, 83, 959–963,
677 doi:10.1785/0220120093, 2012.

678 van Dinther, Y., T. V. Gerya, L. A. Dalguer, F. Corbi, F. Funiciello, and P. M. Mai,
679 The seismic cycle at subduction thrusts: 2. dynamic implications of geodynamic
680 simulations validated with laboratory models, *J. Geophys. Res.-Sol. Ea.*, 118(4),
681 1502–1525, doi:10.1029/2012JB009479, 2013.

682 Viesca, R. C., Stable and unstable development of an interfacial sliding instability,
683 *Phys. Rev. E*, 93, 060,202, doi:10.1103/PhysRevE.93.060202, 2016a.

684 Viesca, R. C., Self-similar slip instability on interfaces with rate- and state-dependent
685 friction, *Proceedings of the Royal Society A: Mathematical, Physical and Engineering*
686 *Sciences*, 472(2192), 20160,254, doi:10.1098/rspa.2016.0254, 2016b.

687 Ward, S. N., ALLCAL Earthquake Simulator, *Seismol. Res. Lett.*, 83(6), 964–972,
688 doi:10.1785/0220120056, 2012.

689 Wei, M., Y. Kaneko, Y. Liu, and J. J. McGuire, Episodic fault creep events in California
690 controlled by shallow frictional heterogeneity, *Nat. Geosci.*, 6, 566–570, doi:10.1038/
691 ngeo1835, 2013.

692 Wei, M., Y. Kaneko, P. Shi, and Y. Liu, Numerical modeling of dynamically triggered
693 shallow slow slip events in New Zealand by the 2016 Mw 7.8 Kaikoura earthquake,
694 *Geophys. Res. Lett.*, 45(10), 4764–4772, 2018.

695 Wollherr, S., A.-A. Gabriel, and P. M. Mai, Landers 1992 "reloaded": Integrative
696 dynamic earthquake rupture modeling, *J. Geophys. Res.-Sol. Ea.*, 2018.

697 Wu, Y., and X. Chen, The scale-dependent slip pattern for a uniform fault model
698 obeying the rate-and state-dependent friction law, *J. Geophys. Res.*, *119*(6), 4890–
699 4906, 2014.

700 Xu, J., H. Zhang, and X. Chen, Rupture phase diagrams for a planar fault in 3-d
701 full-space and half-space, *Geophys. J. Int.*, *202*(3), 2194–2206, 2015.

Table 1: Parameter values used in the benchmark problem

Parameter	Definition	Value, Units
ρ	density	2670 kg/m ³
c_s	shear wave speed	3.464 km/s
σ_n	effective normal stress on fault	50 MPa
a	rate-and-state parameter	variable (see Fig. 1)
b	rate-and-state parameter	variable (see Fig. 1)
L	critical slip distance	BP1: 0.008 m BP2: 0.004 m
V_p	plate rate	10 ⁻⁹ m/s
V_{init}	initial slip rate	10 ⁻⁹ m/s
V_0	reference slip rate	10 ⁻⁶ m/s
f_0	reference friction coefficient	0.6
H	depth extent of uniform VW region	15 km
h	width of VW-VS transition zone	3 km
W_f	width of rate-and-state fault	40 km
Δz	suggested cell sizes	BP1: 25 m BP2: 25 m, 50 m, 100 m, 200 m, 300 m, 400 m, 800 m
t_f	final simulation time	BP1: 3000 years BP2: 1200 years
L_z	depth of computational domain	<i>not specified</i>
L_x	off-fault distance of computational domain	<i>not specified</i>

Table 2: Details of participating SEAS codes and modeling groups.

Code Name	Type	Modeler Name & Group Members	References
SCycle	FDM	abrahams (Abrahams/ Allison/Dunham)	<i>Erickson and Dunham (2014)</i> <i>Allison and Dunham (2018)</i> https://github.com/kali-allison/SCycle
FDCycle	FDM	erickson (Erickson/Mckay)	<i>Erickson and Dunham (2014)</i> https://github.com/brittany-erickson/FDCycle
QDESDG	DG-FEM	kozdon (Kozdon)	https://github.com/jkozdon/QDESDG
Unicycle	BEM	barbot (Barbot)	<i>Barbot (2019)</i> http://bitbucket.org/sbarbot
FDRA	BEM	cattania (Cattania/Segall)	<i>Segall and Bradley (2012b)</i> ; <i>Bradley (2014)</i>
BICycle	BEM	jiang (Jiang) lambert (Lambert/Lapusta) xma (Ma/Elbanna)	<i>Lapusta et al. (2000)</i> ; <i>Lapusta and Liu (2009)</i>
QDYN	BEM	luo (Luo/Idini/ van den Ende/Ampuero)	<i>Luo and Ampuero (2017)</i> https://github.com/ydluo/qdyn
ESAM	BEM	liu (Liu) wei (Wei/Shi)	<i>Liu and Rice (2007)</i>

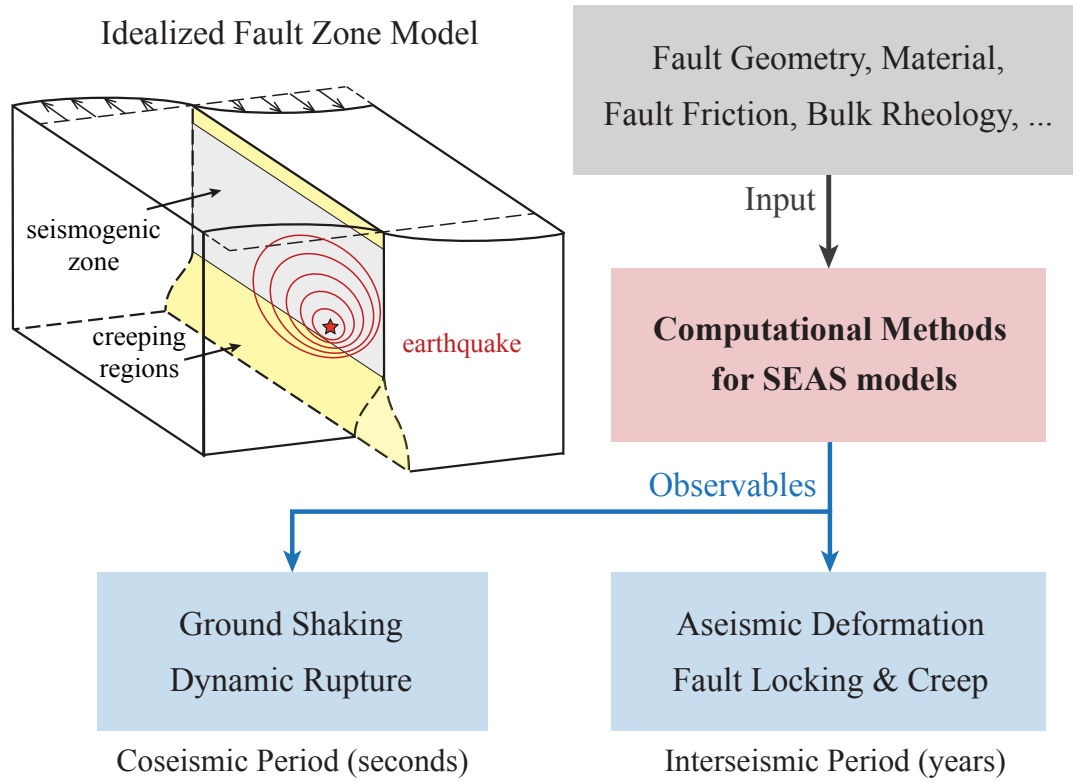


Figure 1: Ingredients and observables for SEAS (sequences of earthquakes and aseismic slip) models. In a conceptual fault-zone model, earthquakes initiate at seismogenic depths (red star) and rupture through the interseismically locked regions (gray), while aseismic slip occurs in deeper and sometimes shallower regions (yellow). For numerical models, given fault zone properties, computational simulations can reproduce long-term fault locking and creep over years to decades, punctuated by dynamic earthquake ruptures over seconds to minutes. Seismic shaking and aseismic deformation are typical observables from the surface.

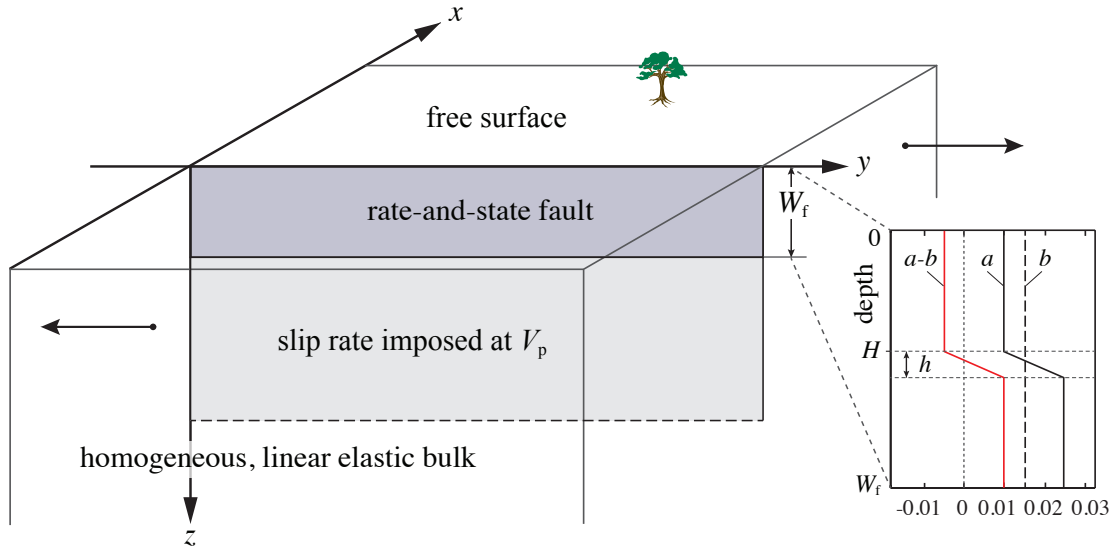


Figure 2: Our first SEAS benchmark is based on the model in *Rice (1993)*, where a planar fault is embedded in a homogeneous, linear elastic half-space with a free surface. A vertical cross-section of the 3D setting is taken so that slip varies only with depth and deformation is 2D antiplane strain. The fault is governed by rate-and-state friction with depth-dependent frictional parameters a and b above the depth W_f , below which a steady slow loading rate V_p is assumed. The friction-controlled fault is seismogenic due to velocity-weakening properties ($(a - b) < 0$) down to depth H and accommodates aseismic creep at greater depths due to velocity-strengthening properties ($(a - b) > 0$). Earthquakes nucleate spontaneously, with inertia approximated with radiation damping.

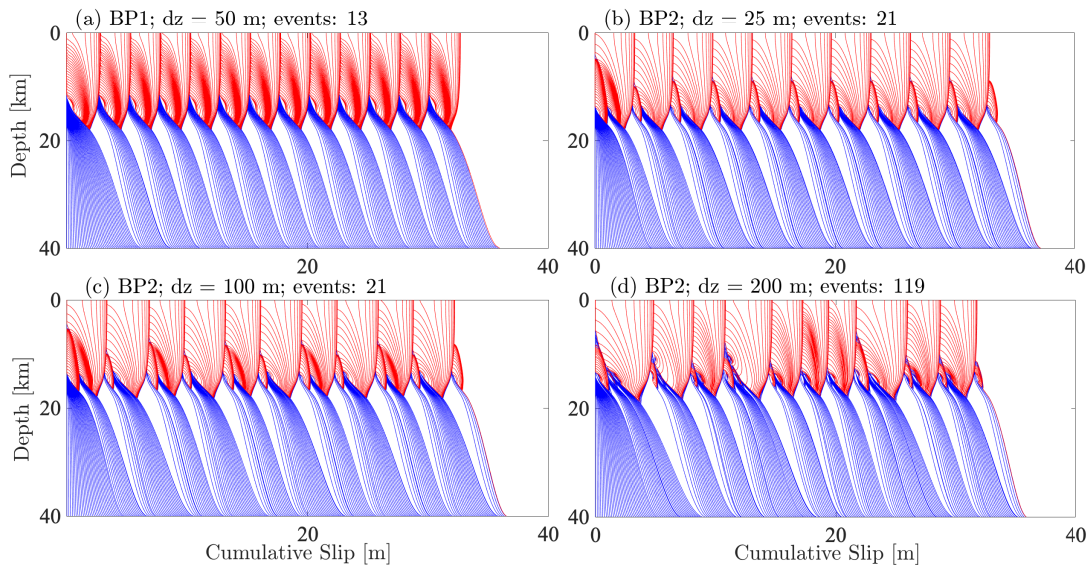
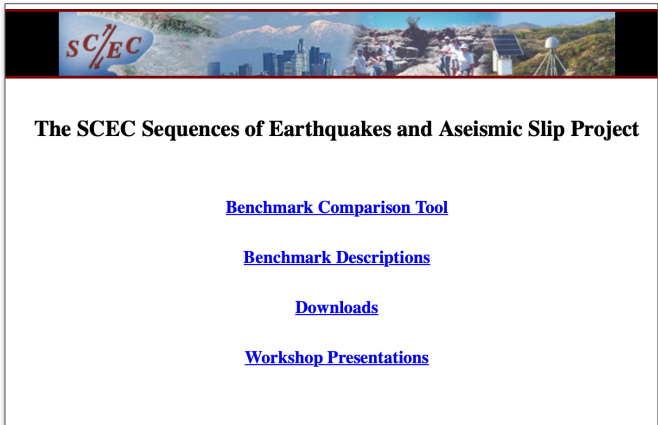


Figure 3: Cumulative slip profiles plotted over a 1,200 year period in blue every 5 years during interseismic loading and in red every second during quasi-dynamic rupture. Results were obtained using the BICyclE code for (a) BP1 with a cell size of 50 m, (b) BP2 with a cell size of 25 m, (c) BP2 with a cell size of 100 m and (d) BP2 with a cell size of 200 m. Number of events also listed, where we define a seismic event to be one with a local slip rate > 0.01 m/s separated by aseismic periods of at least 15 s.



Benchmarks			
Name	Date	Description	Action
bp1	4/14/2018 8:08 AM	2D Antiplane Shear	Select
bp2	10/6/2018 6:20 AM	2D Antiplane Shear, Varying Cell Size	Select

Users				
			Select Checked	Select All
Name	Description	Action		
<input type="checkbox"/>	abrahams	100 km X 80 km: Free surface outer BC	Select	
<input type="checkbox"/>	abrahams.2	100 km X 80 km: Vp/2 outer BC	Select	
<input type="checkbox"/>	abrahams.3	400 km X 200 km: Vp/2 outer BC	Select	
<input type="checkbox"/>	barbot	Sylvain Barbot (Fortran90)	Select	
<input type="checkbox"/>	barbot.2	Sylvain Barbot (Matlab)	Select	
<input type="checkbox"/>	cattania	Camilla Cattania - fdra (bem)	Select	
<input type="checkbox"/>	cattania.2	Camilla Cattania - fdra (fft, 160 km)	Select	
<input type="checkbox"/>	cattania.3	Camilla Cattania - fdra (fft, 640 km)	Select	
<input type="checkbox"/>	erickson	Brittany Erickson	Select	
<input type="checkbox"/>	erickson.2	Brittany Erickson	Select	

Figure 4: Online platform for the SEAS working group. (Left) Home page for our website. (Top right) Currently available benchmarks. (Bottom right) Examples of BP1 model submissions.

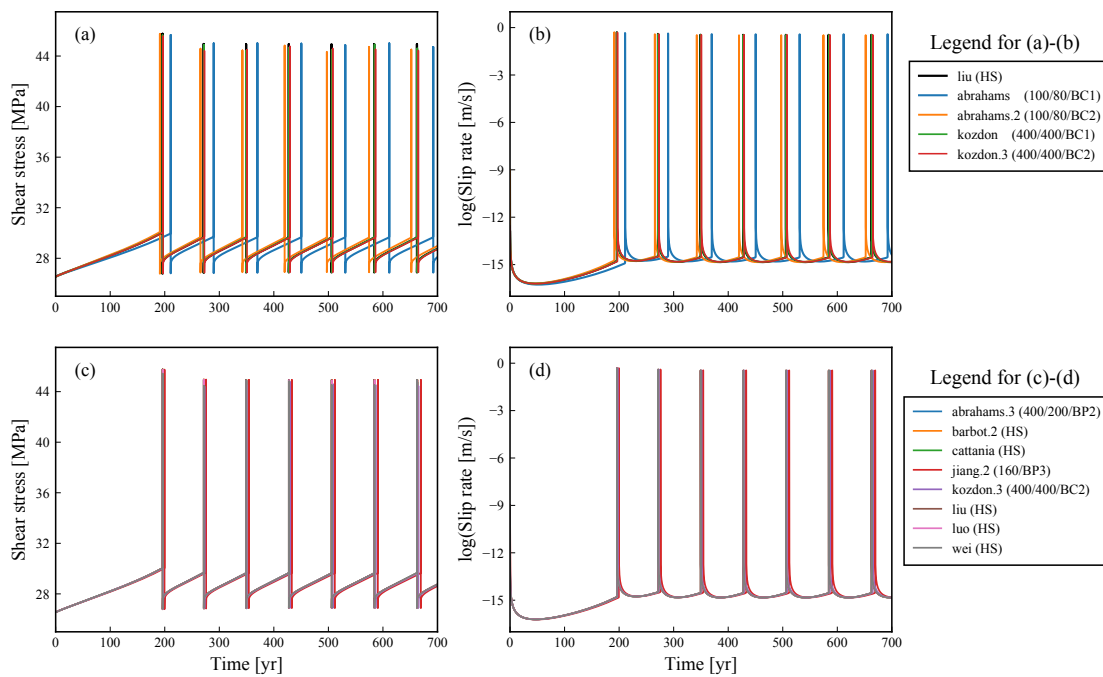


Figure 5: Long-term behavior of BP1 models. (a) Shear stress and (b) slip rates at the depth of 7.5 km in models with different outer boundary conditions (BC) and computational domain sizes. (c) Shear stress and (d) slip rates at depth of 7.5 km in models with sufficiently large computational domain sizes. Legend labels indicate model names followed by information on BC and domain size, namely, $(L_x/L_z/BC)$ for FDM/FEM, and (L_z/BC) or (HS, half-space) for BEM. BC1 and BC2 refer to the far-field free surface or displacement BC and BC3 refers to the periodic BC.

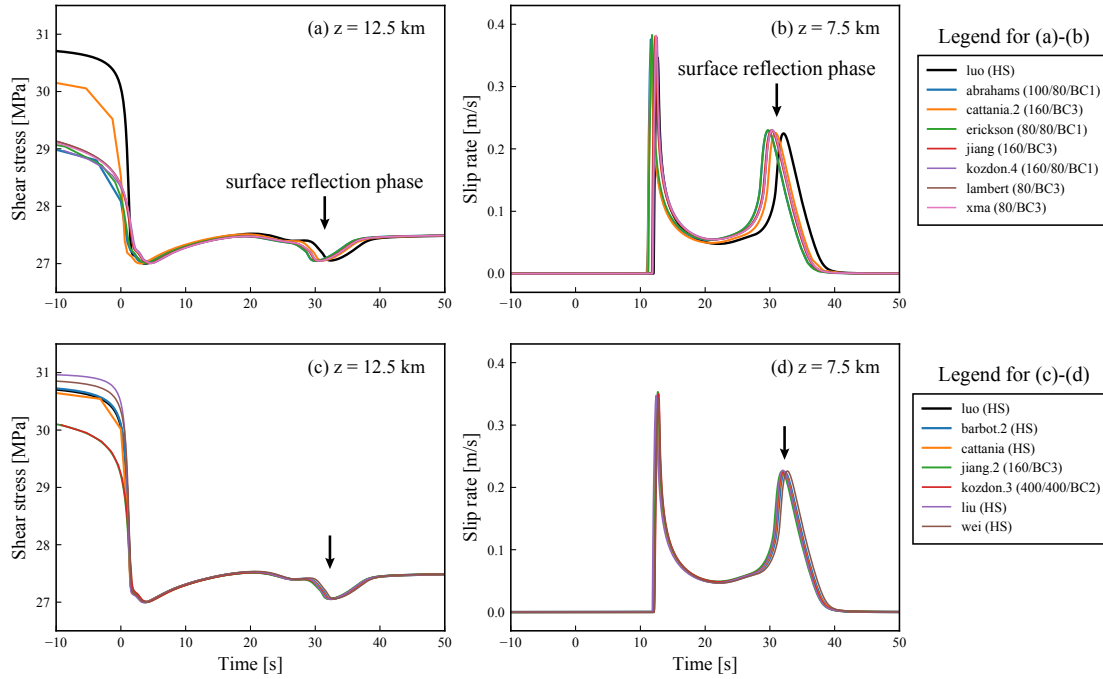


Figure 6: Coseismic behavior of BP1 models. Coseismic phase during the 8th event in Figure 5 is shown. Models with smaller computational domain sizes show discrepancies in (a) shear stresses at 12.5km depth and (b) slip rates at 7.5km depth. Models with sufficiently large computational domain sizes are compared for (c) shear stresses at 12.5km depth and (d) slip rates at 7.5km depth. Time series are aligned relative to the rupture initiation time at the depth of 12.5 km in each model. Note that the half-space solution **luo** is the same in (b) and (d) and serves as a reference. The surface reflection phase is marked by a black arrow.

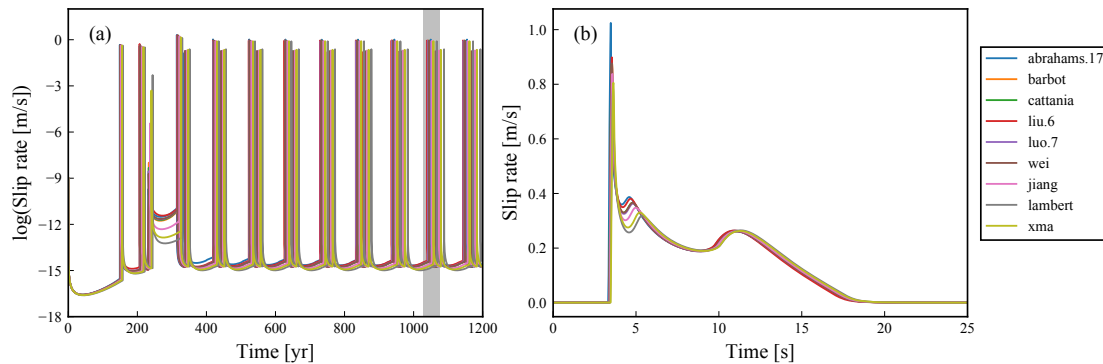


Figure 7: Comparison of best-resolved BP2 models (cell size of ~ 25 m). (a) Long-term evolution of slip rates at depth of 9.6 km; (b) coseismic evolution of slip rates at the depth of 9.6 km for the 10th large events in the sequence (marked in gray in (a)). Time series are aligned relative to the rupture initiation time at the depth of 12 km in each model.

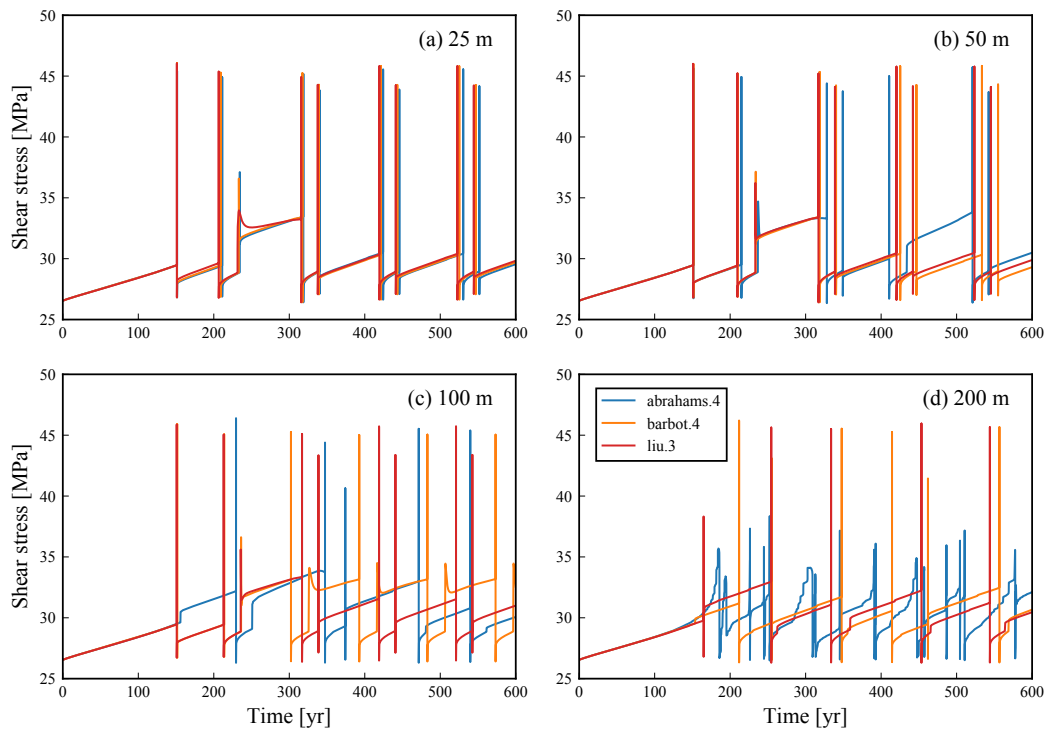


Figure 8: Increasing discrepancy in BP2 models due to an increased cell size of (a) 25 m, (b) 50 m, (c) 100 m, and (d) 200 m. Time evolution of shear stress at the depth of 9.6 km during the first 600 years is shown for models from three groups (**abrahams**, **barbot**, and **liu**).

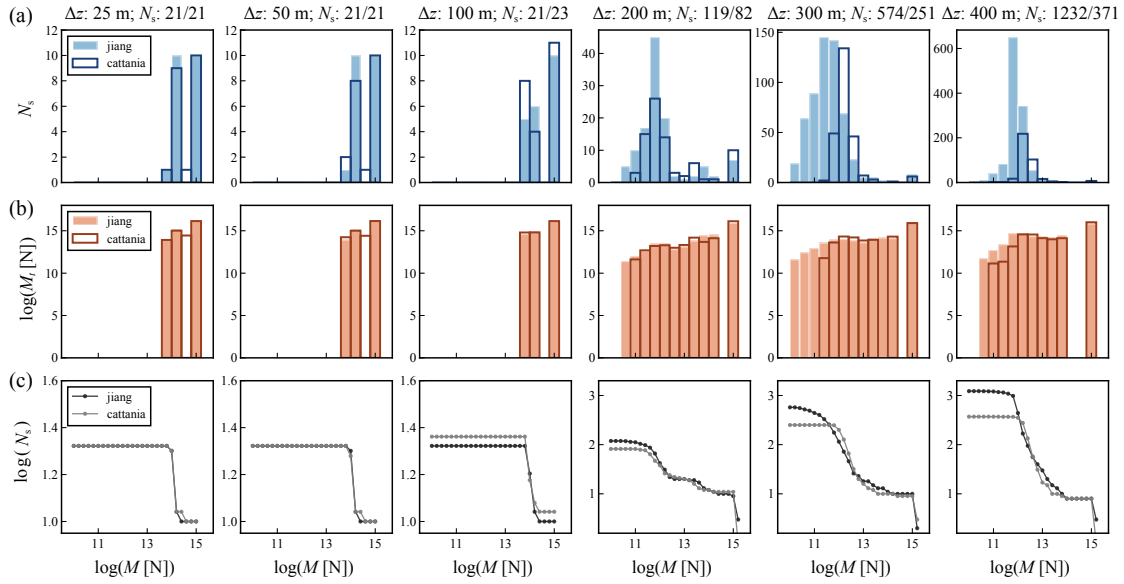


Figure 9: Effect of model resolution on earthquake patterns. Distribution of (a, top row) earthquake sizes and (b, middle row) of total seismic moment release per unit length, M (in unit of N) and (c, bottom row) frequency-size relation. Models from two groups (**jiang** and **cattania**) are compared. The corresponding cell size (Δz) and total seismic event numbers (N_s) are marked in the titles. Seismic moment M refers to the seismic moment of each earthquake; total seismic moment M_t refers to the sum of moment release for all earthquakes within each magnitude bin. N_s in (c) refers to the number of seismic events with moment above the corresponding M .

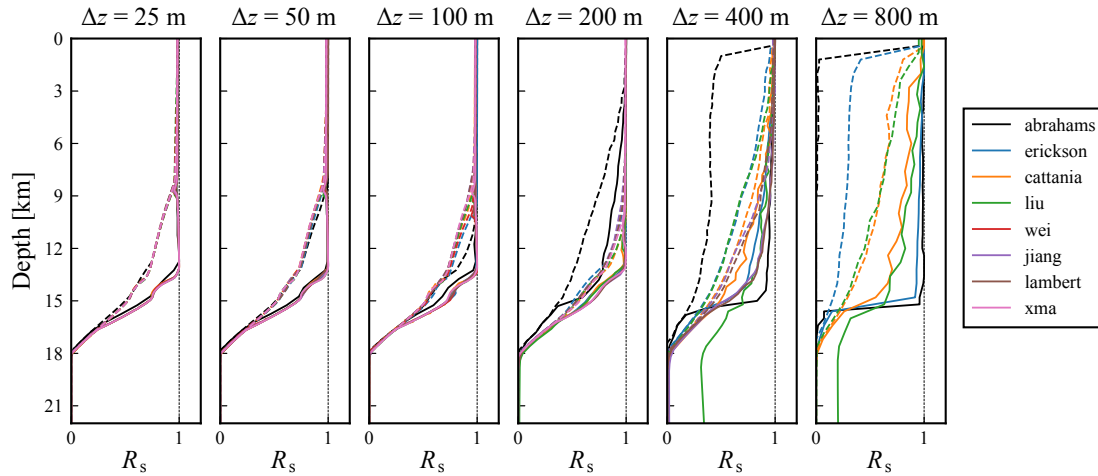


Figure 10: Effect of model resolution on seismic-aseismic slip partitioning over depth. Depth distribution of the ratio of total seismic moment release to total moment release, R_s , is shown by solid lines. The ratio between seismic moment due to surface-breaching earthquakes (with surface slip greater than 0.1 m) to total moment release is indicated by dashed lines. Simulations with different resolutions are shown, with the same color for each modeling group. Note that not all groups have simulation results for all resolutions.

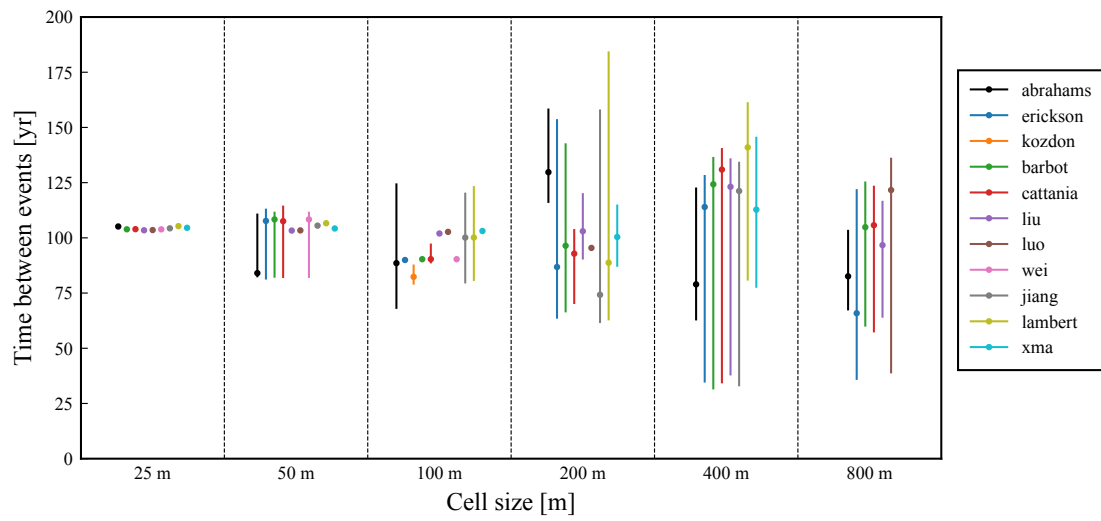


Figure 11: Effect of model resolution on recurrence intervals of large surface-breaching events. The vertical lines indicate the range of recurrence interval values, with the median value marked as dots.